A Semianalytical Parameter-Extraction Procedure for HBT Equivalent Circuit

Bin Li, *Student Member, IEEE,* Sheila Prasad, *Senior Member, IEEE,* Li-Wu Yang, *Senior Member, IEEE,* and S. C. Wang

***Abstract*— A parameter-extraction approach for the heterojunction bipolar transistor (HBT), which combines the analytical approach and empirical optimization procedure, is developed. The extraction techniques for extrinsic base–collector capacitance and pad parasitics are also included in this approach. The cutoff operation of the HBT's is utilized to extract the values of the pad capacitances. An excellent fit between measured and simulated S-parameters in the frequency range of 50 MHz–36 GHz is obtained over a wide range of bias points.**

***Index Terms*— Heterojunction bipolar transistor, parameter extraction, semianalytical method.**

I. Introduction

HETEROJUNCTION bipolar transistors (HBT's) have been used for digital, analog, and power applications due to their superior high-speed and high-current driving capabilities. An accurate physically significant HBT model is very important for designing a circuit, evaluating the process technology, and optimizing the design of the device. The analytical approach in HBT equivalent-circuit parameter extraction has been recently addressed. A direct extraction procedure was presented in [1], where special test structures were designed for the parasitic parameters. The frequency dependence of the network parameters of the equivalent circuit was discussed in [2], allowing a direct evaluation of most element parameters. A fully analytical approach for extracting all the parameters was given in [3], where certain assumptions and local optimizations were used. More recently, the combination of an analytical approach and optimization procedure was established in [4], where a distributed base–collector capacitance was included. Certain constraints and element values derived from the analytical approach used to extract the parameters of InP-based HBT's were presented in [5]. Another direct extraction procedure for HBT's was developed in [6], where S-parameter data measured under open-collector bias conditions were utilized to obtain the extrinsic elements and a distributed base–collector capacitance was included. Finally, an approach combining analytical and optimization parameter evaluation was reported in [7], in which dc and multibias RF information is used to evaluate the model parameters by the conditioned impedance-block optimization.

Most of the direct extraction techniques used the deembedded small-signal equivalent circuits [3], [4], [6], [8] to extract some model parameters based on the frequency behavior of the deembedded equivalent circuit. These extraction procedures are based on certain assumptions and approximations. Due to the diversity of the process technology, device design, and geometry, these assumptions and approximations need to be modified and adjusted for specific devices. In this paper, an extraction approach combining the analytical and optimization approaches is presented. An HBT equivalent circuit includes the extrinsic base–collector capacitance and pad capacitances. The pad capacitances are extracted from S-parameters of the HBT's under cutoff operation. The behavior of the deembedded Z-parameters is then analyzed to extract all the parameters, except the base extrinsic and intrinsic resistances $R_{\rm bi}$, $R_{\rm bx}$. The constraint for the base resistances is obtained from analysis and used in the optimization procedure to extract the exact values of $R_{\rm bx}$ and $R_{\rm bi}$ The small-signal model parameters at multiple biases were extracted, and errors between measurement and simulation are given to verify the validity of this approach. The influence of the pad parasitics is also given to explain the importance of considering the parasitics.

Section II gives the small-signal equivalent circuit of HBT's, basic formalism, and approximations used in the extraction procedure. Section III discusses the basic procedure for extracting the small-signal element parameters. Section IV gives the extraction result and discussion. The conclusion is given in Section V.

II. Theoretical Analysis

The AlGaAs/GaAs common-emitter HBT with an emitter area of 30 μm^2 was used in this investigation. The small-signal equivalent circuit used for this paper is the T-model shown in Fig. 1. The dashed box in Fig. 1 indicates the inner shell without the pad parasitics. The Z-parameters presented below are all for the inner shell. There are 16 elements in the equivalent circuit. Only $C_{\rm be}$, r_e, α, $R_{\rm bc}$, and $C_{\rm bc}$ are considered to be bias dependent and all the other elements are assumed to be bias independent. The expressions for the two-port Z-parameters of the inner shell can be simplified in terms of the frequency ranges. The frequency

Manuscript received September 15, 1997. The work of S. Prasad was supported in part by the National Science Foundation under Grant ECS-9529643.

B. Li was with the Department of Electrical and Computer Engineering, Northeastern University, Boston, MA 02115 USA. He is now with Vitesse Semiconductor Corporation, Camarillo, CA 93012 USA.

S. Prasad is with the Department of Electrical and Computer Engineering, Northeastern University, Boston, MA 02115 USA.

L.-W. Yang is with TRW, Inc., Redondo Beach, CA 90278 USA.

S. C. Wang is with Lockheed Sanders, Nashua, NH 03060 USA.

Publisher Item Identifier S 0018-9480(98)07245-7.

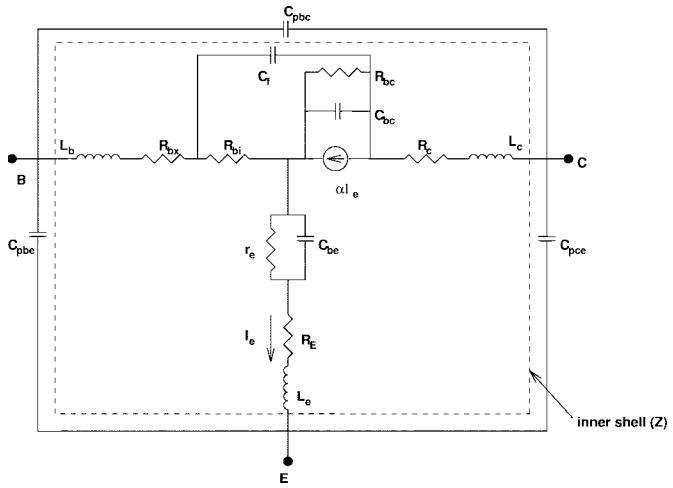

Fig. 1. The small-signal equivalent circuit of the AlGaAs/GaAs HBT's.

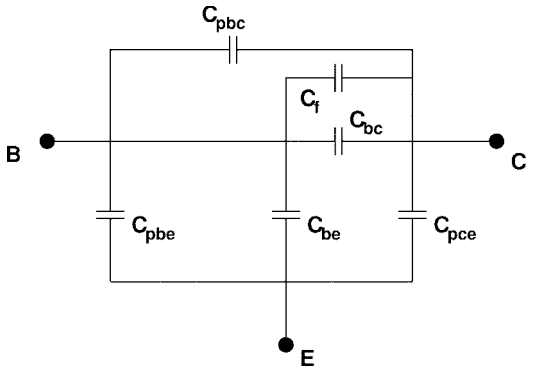

Fig. 2. The simplified HBT equivalent circuit under cutoff operations in which both junctions are reverse-biased and the influence of the inductances and resistances remains negligible.

ranges are characterized by $\omega C_{\rm bc}R_{\rm bc} \ll 1$ (low-frequency range), $\omega C_{\rm bc}R_{\rm bi}$, $\omega C_f R_{\rm bi} \ll 1$ and $\omega C_{\rm bc}R_{\rm bc} \gg 1$ (middle-frequency range), and $\omega C_{\rm bc}R_{\rm bi} \gg 1$ (high-frequency range). In the measurements, most of the frequency data are located in the middle-frequency range. In the low-frequency range, we have

$$Z_{11} - Z_{12} = R_{\rm bx} + j\omega L_b + R_{\rm bi} - j\omega R_{\rm bc}R_{\rm bi}C_s \tag{1}$$

$$\begin{aligned} Z_{12} = {} & R_E + j\omega L_e + r_e - j\omega r_e^2 C_{\rm be} \\ & + (1-\alpha) \times j\omega R_{\rm bi}C_f(R_{\rm bc} - j\omega R_{\rm bc}^2 C_s) \end{aligned}$$

$$Z_{22} - Z_{21} = R_C + j\omega L_c + R_{\rm bc} - j\omega R_{\rm bc}^2 C_s \tag{2}$$

where $C_s = C_{\rm bc} + C_f$.

In the middle-frequency range, the Z-parameters can be approximated as

$$Z_{11} - Z_{12} = R_{\rm bx} + j\omega L_b + R_{\rm bi}\frac{C_{\rm bc}}{C_s} \tag{3}$$

$$\begin{aligned} Z_{12} = {} & R_E + j\omega L_e + r_e - j\omega r_e^2 C_{\rm be} + (1-\alpha) \\ & \times R_{\rm bi} \times \frac{C_f}{C_s} \end{aligned} \tag{4}$$

$$\begin{aligned} Z_{22} - Z_{21} = {} & R_C + j\omega L_c + \frac{1}{j\omega C_s} + \frac{1}{\omega^2 R_{\rm bc}C_s} \\ & - \frac{R_{\rm bi}C_{\rm bc}C_f}{C_s^2} - j\frac{R_{\rm bi}C_f C_{\rm bc}}{\omega C_s^3 R_{\rm bc}}. \end{aligned} \tag{5}$$

In the high-frequency range, the simplified relation is

$$\begin{aligned} Z_{22} - Z_{21} = {} & R_C + j\omega L_c - \frac{1}{\omega^2 R_{\rm bi}C_{\rm bc}C_f} + \frac{1}{\omega^2 R_{\rm bi}C_{\rm bc}C_f} \\ & \cdot\left(\frac{1}{j\omega C_f R_{\rm bi}} + \frac{1}{j\omega C_{\rm bc}R_{\rm bi}}\right) \end{aligned} \tag{6}$$

where $\alpha = \alpha_0[1/(1+j\omega/\omega_0)]\,e^{-j\omega\tau}$.

For the device under investigation, the middle-frequency range is approximately from 0.5 to 20 GHz, the high-frequency range should go up to 40 GHz. Since the maximum frequency measured is 36 GHz, the condition for the high frequency is relaxed and frequencies over 25 GHz were considered to be in the high-frequency range.

III. Parameter Extraction

A. Extraction of the Parasitic Elements

If no test structure is available for extracting the parasitics, the pad capacitances can be extracted or estimated from HBT's under cutoff operation [7], [9]. Under such conditions, the HBT equivalent circuit of Fig. 1 is reduced to capacitive elements only, and can be simplified, as shown in Fig. 2, as long as the influence of the inductances and resistances remains negligible and the conditions $R_{\rm bc} \gg (1/\omega C_{\rm bc})$ and $R_{\rm be} \gg (1/\omega C_{\rm be})$ are satisfied.

The capacitances in the equivalent circuit can be directly calculated by

$$C_{\rm pbe} + C_{\rm be} = \frac{{\rm Im}(Y_{11}) + {\rm Im}(Y_{12})}{\omega} \tag{7}$$

$$C_{\rm pce} = \frac{{\rm Im}(Y_{22}) + {\rm Im}(Y_{12})}{\omega} \tag{8}$$

$$C_{\rm pbc} + C_f + C_{\rm bc} = -\frac{{\rm Im}(Y_{12})}{\omega}. \tag{9}$$

In the above equations, the $C_{\rm pbe}$, $C_{\rm pbc}$, $C_{\rm pce}$, and C_f are considered to be bias independent and $C_{\rm be}$ and $C_{\rm bc}$ are bias-dependent elements. The value of $C_{\rm pce}$ can be calculated from (8). The result is shown in Fig. 3, and it is obvious that the $C_{\rm pce}$ is bias independent. The calculated average value of $C_{\rm pce}$ is 41 fF.

$C_{\rm be}$, the base–emitter junction capacitance, can be described by

$$C_{\rm be} = \frac{C_{\rm jbe0}}{(1 + V_{EB}/V_{\rm jbe})^{M_{\rm jbe}}}. \tag{10}$$

The extraction of $C_{\rm pbe}$ can be carried out by fitting the sum of $C_{\rm pbe}+C_{\rm be}$ to (10) at different reverse base–emitter voltages or by using the iteration method in which different values of $V_{\rm jbe}$, $M_{\rm jbe}$, and $C_{\rm jbe0}$ are tried until the plot of $(C_{\rm pbe}+C_{\rm be})$ versus $(1+V_{EB}/V_{\rm jbe})^{-M_{\rm jbe}}$ is a straight line. The result is shown in Fig. 4. The value of $C_{\rm pbe}$ is 27.4 fF.

Similarly, $(C_f + C_{\rm pbc})$ can be extracted by fitting the sum $(C_f + C_{\rm pbc} + C_{\rm bc})$ to the expression for junction capacitance at different base–collector voltages. The result is $(C_f + C_{\rm pbc}) = 16.5$ fF. However, it must be noted that it is difficult to

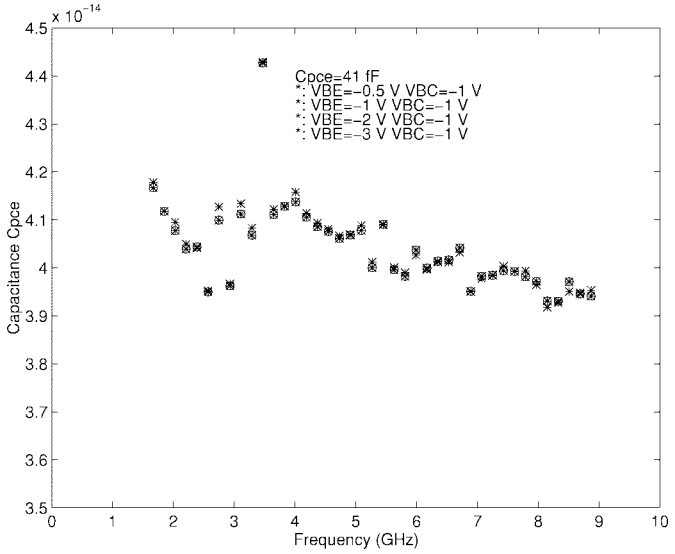

Fig. 3. The calculated $C_{\rm pce}$ versus frequency.

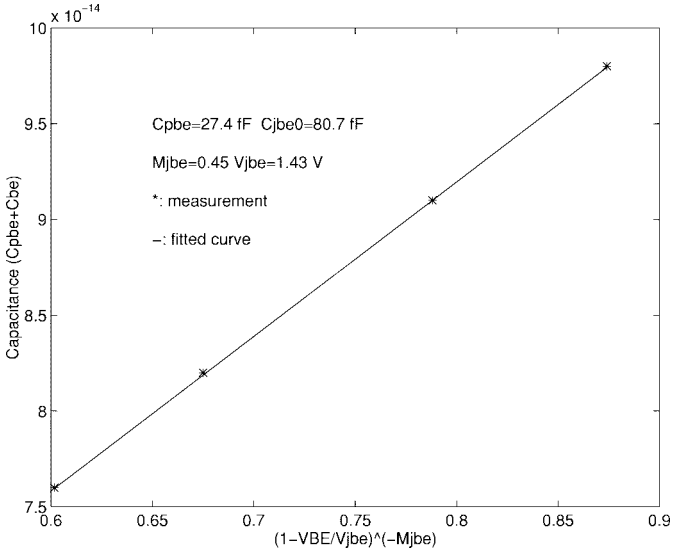

Fig. 4. The fitting of the sum ($C_{\rm pbe}+C_{\rm be}$) to the expression for junction capacitance.

distinguish between the base–collector coupling capacitance and extrinsic base–collector capacitance [7]. The reason is that the distance between the base probe tip and collector probe tip is longer and, thus, the coupling effect between base and collector contact must be very small; furthermore, the influence of $C_{\rm pbc}$ can be absorbed by the extrinsic base–collector capacitance C_f. Thus, $C_{\rm pbc}$ was chosen to be zero. Such an assumption is also confirmed by the empirical optimization procedures.

The S-parameters measured over the frequency range of 50 MHz–36 GHz were first converted to Y-parameters. After deembedding the effect of the pad capacitances, the Y-parameters of the inner shell are converted to Z-parameters. Most of the elements are extracted from an analysis of the behavior of the Z-parameters. Certain constraints are obtained to help in conditioning the optimization procedure and to reduce the uncertainty.

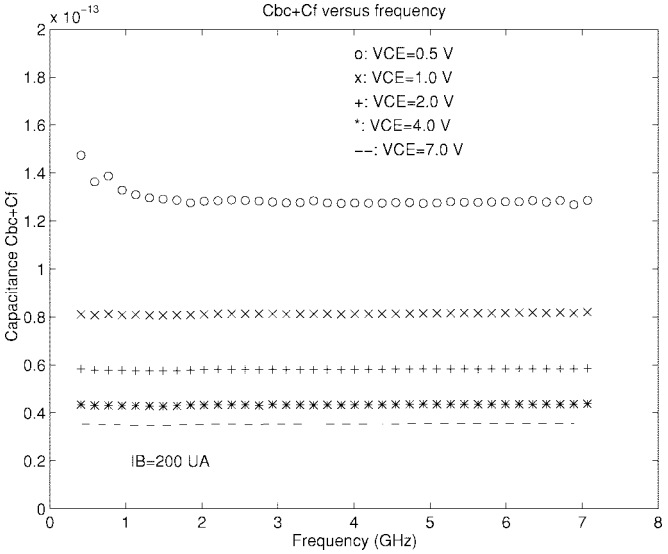

Fig. 5. The extracted value $C_{\rm bc}$ at different base–collector voltages.

B. The Base–Collector Capacitance C_s

As indicated in (5), we have the following approximation in the middle-frequency range:

$$\mathrm{Im}(Z_{22}-Z_{21}) = j\omega L_c + \frac{1}{j\omega C_s} - j\frac{R_{\rm bi}C_fC_{\rm bc}}{\omega C_s^3 R_{\rm bc}}. \qquad (11)$$

At the low end of the middle-frequency range, the second term is much greater than the other terms on the right-hand side of the equation. C_s can be extracted by

$$C_s = \frac{1}{\omega\,\mathrm{Im}(Z_{22}-Z_{21})}. \qquad (12)$$

The extracted C_s from (12) at the bias values for $V_{\rm CE} = \{0.5\,\mathrm{V},\ 1.0\,\mathrm{V},\ 2.0\,\mathrm{V},\ 4.0\,\mathrm{V},\ 7.0\,\mathrm{V}\}$, and $I_B = 200\ \mu\mathrm{A}$ is shown in Fig. 5. At $V_{\rm CE} = 0.5$ V, $1/\omega C_s \simeq 1224\ \Omega$, which is much larger than the other terms in the middle-frequency range if the values extracted below are used. It is also noted that the base–collector capacitances decrease as the $V_{\rm CE}$ increases. This results from the increased width of the base–collector depletion region due to the increased $V_{\rm CE}$. The deviation of C_s is less than 5% with the exception of $V_{\rm CE} = 0.5$ V. This is because the base–collector junction is forward biased at $V_{\rm CE} = 0.5$, and the middle-frequency range moves up.

The extrinsic base–collector capacitance is generally a weak function of the base–collector-junction voltage. In extreme cases, it can be considered to be independent of the bias variation, or the ratio of the extrinsic capacitance to the total base–collector capacitance is considered to be a constant. Practically speaking, the extrinsic capacitance C_f is the in-between case. In this paper, for simplicity, the extrinsic capacitance is considered to be fixed and extracted from the values of C_s at the different base–collector voltages. A method similar to that used for the extraction of the value of $C_{\rm pbe}$ and $C_{\rm pce}$ is applied here. The value of C_s is 16.5 F, which agrees with that from the cutoff measurement. The parameters

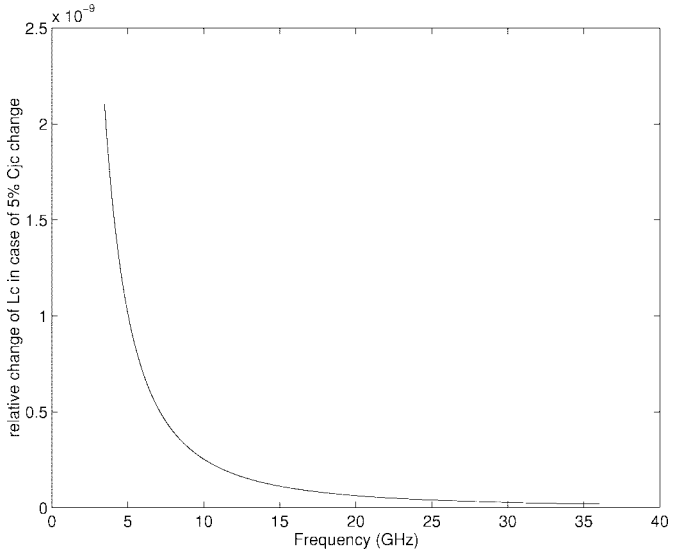

Fig. 6. The variation of L_c with a 5% error in the estimation of C_s.

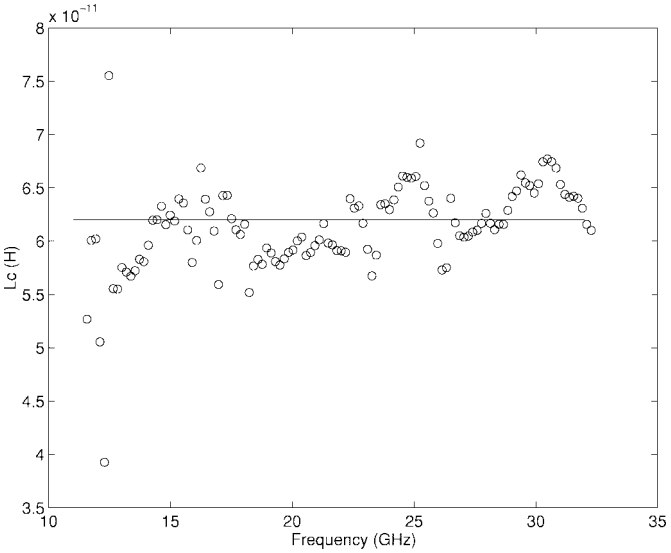

Fig. 7. The extracted L_c versus frequency.

for base–collector-junction capacitance are also extracted from this approach: $C_{jc0} = 54.7$ fF, $V_{jc} = 1.30$ V, and $M_{jc} = 0.63$.

C. The Collector-Contact Lead Inductor L_c

The collector lead conductor L_c can be calculated by (11)

$$L_c = 1/\omega\left\{\mathrm{Im}(Z_{22} - Z_{21}) + \frac{1}{\omega C_s}\right\}. \tag{13}$$

The third term in (11) is assumed to be small enough and is neglected. This straightforward method is not as accurate as expected. The deviation of the extracted value of L_c is large, and an accurate value of L_c is difficult to obtain. The reason is that the small error resulting from extracting C_s could lead to large errors in L_c. We differentiate (13) and obtain

$$\Delta L_c = \frac{1}{\omega^2}\left(-\frac{1}{C_s^2}\right)\Delta C_s = -\frac{1}{\omega^2 C_s} \times \frac{\Delta C_s}{C_s}. \tag{14}$$

Assuming a 5% error exists in the extraction of C_s and $C_s = 5 \times 10^{-14}$, the error in estimating L_c resulting from the error in the estimation of C_s is plotted in Fig. 6. It is shown that L_c is very sensitive to the error in extracting C_s.

It is also noted that L_c is less sensitive to the error in estimating C_s if the magnitude of C_s becomes larger. Therefore, a good bias point to extract L_c would be zero bias, at which the third term in the equation is negligible and the value of C_s is larger. The L_c extracted at zero bias is shown in Fig. 7.

D. The Base–Collector Resistance R_{bc}

The real part of $Z_{22} - Z_{21}$ in the middle-frequency range is given by

$$\mathrm{Re}(Z_{22} - Z_{21}) = R_c + \frac{1}{\omega^2 R_{\mathrm{bc}} C_s} - \frac{R_{\mathrm{bi}} C_{\mathrm{bc}} C_f}{C_s^2}. \tag{15}$$

If the term $(1/\omega^2 R_{\mathrm{bc}} C_s)$ is much larger than the other two terms, R_{bc} can be approximately extracted from the real part

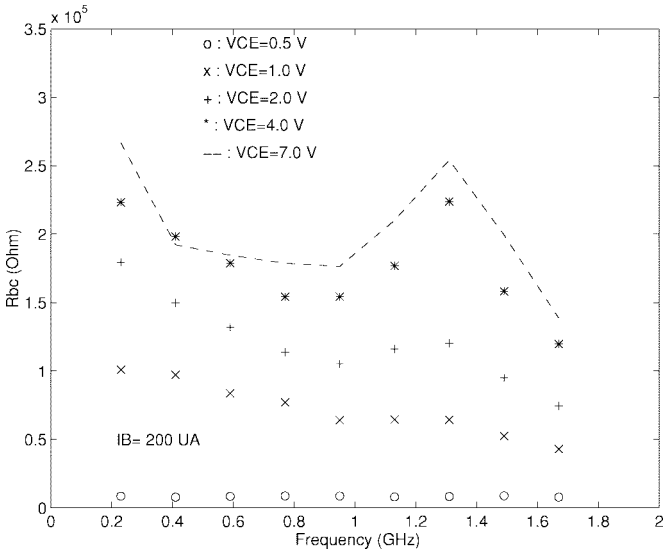

Fig. 8. The extracted R_{bc} at different base–collector voltages.

of $Z_{22} - Z_{21}$ in the lower middle-frequency range as follows:

$$R_{\mathrm{bc}} = \frac{1}{\omega^2 C_s \mathrm{Re}(Z_{22} - Z_{21})}. \tag{16}$$

The second term in (15) is inversely proportional to ω^2, therefore, the magnitude of the second term decreases rapidly. The other two terms cannot be neglected as the frequency increases to a certain point. However, the extracted value of R_{bc} is not significant since the value of R_{bc} is very large and does not affect the frequency response much, as long as we are only concerned with forward operation. Fig. 8 shows the extracted R_{bc} at the bias $I_B = 200$ μA and $V_{\mathrm{CE}} = \{0.5\,\mathrm{V}, 1.0\,\mathrm{V}, 2.0\,\mathrm{V}, 4.0\,\mathrm{V}, 7.0\,\mathrm{V}\}$. It is noted that the magnitude of R_{bc} increases as V_{CE} increases. Fig. 9 shows the extracted R_{bc} without deembedding the pad capacitances at the bias $V_{\mathrm{CE}} = 1.0$ V, $I_B = 200$ μA. The magnitude of the calculated R_{bc} is negative beyond 1 GHz. This shows

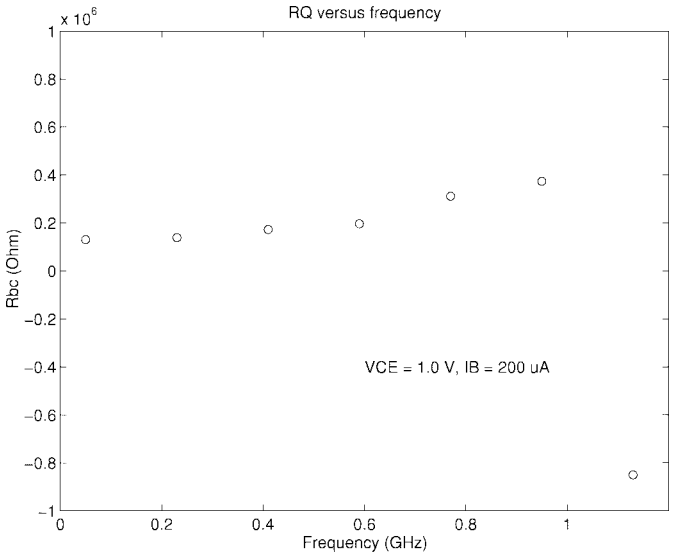

Fig. 9. The extracted $R_{\mathrm{b\,c}}$ at the bias $I_B = 200\ \mu$A, $V_{\mathrm{CE}} = 1.0$ V without deembedding the pad capacitances.

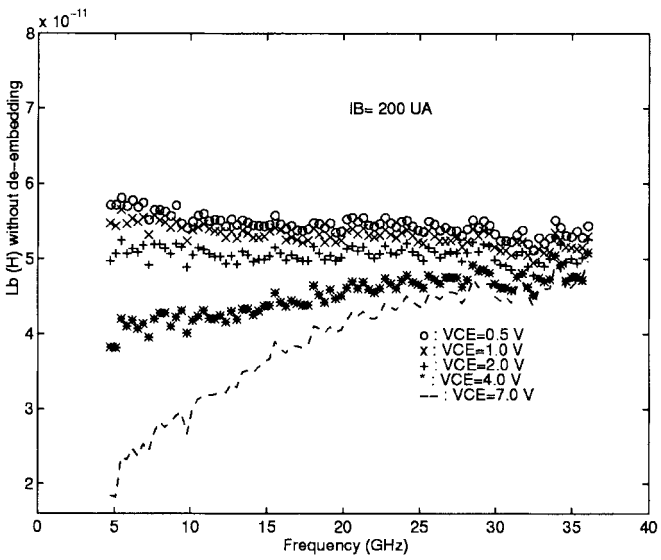

Fig. 10. The L_b versus frequency, in which the pad capacitances have not been deembedded.

that physically meaningless values may be obtained if no deembedding procedure is carried out.

E. The Collector Extrinsic Resistance R_c

The R_c could be extracted by plotting $\mathrm{Re}(Z_{22}-Z_{21})$ versus $1/\omega^2$ in the high-frequency range. The Y-axis intercept is the value of R_c. The requirement for the high-frequency range is difficult to be achieved and the conditions for the requirement are relaxed. C_s is bias dependent, and the larger value of C_s could be achieved from S-parameters at zero bias. R_c should be extracted from zero bias by this method since the R_c is more significant in (6) at zero bias. The extracted value of R_c is 4.99 Ω.

F. The Base-Contact Lead Inductor L_b

From the first-order approximation, L_b could be easily extracted from imaginary part of $Z_{11} - Z_{12}$ in the middle-frequency range. That is

$$L_b = \mathrm{Im}(Z_{11} - Z_{12})/\omega. \tag{17}$$

The extracted L_b at different biases is shown in Fig. 10 without the deembedding procedure. The dependence of the value of L_b on the bias V_{CE} is attributable to the pad capacitance. After the deembedding procedure is carried out, the extracted L_b is shown in Fig. 11. The magnitude variation of L_b at the different biases is very small and almost negligible, and can be considered to be independent of bias. The extracted value of L_b is 55 pH.

G. The Intrinsic and Extrinsic Base Resistances

In principle, the sum of the intrinsic and extrinsic base resistances $R_{\mathrm{bx}}+R_{\mathrm{bi}}$ can be extracted from the low-frequency data, and extrinsic base resistance R_{bx} can be extracted from the high-frequency data if the equivalent circuit shown in Fig. 1 describes the frequency response of the HBT's accurately. However, most of the frequency data are located

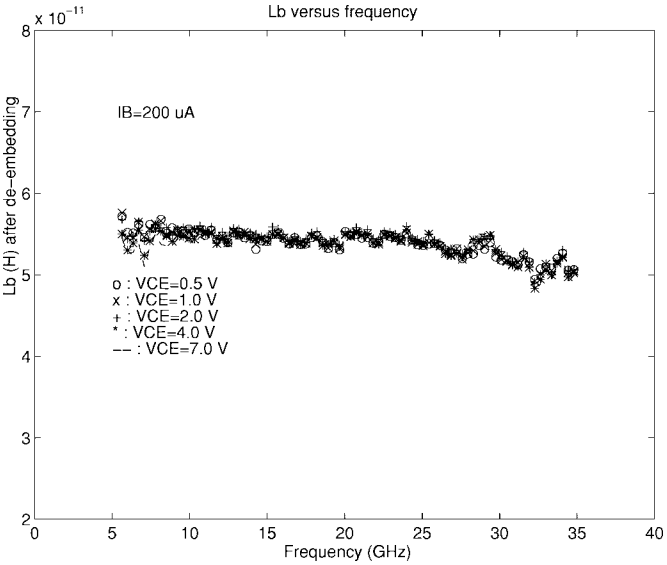

Fig. 11. The L_b versus frequency, in which the pad capacitance effect has been deembedded.

in the middle-frequency range. The requirement for the high-frequency condition is difficult to be satisfied, and the data at extremely low frequencies are not available. The constraints for the base resistances can thus be obtained from the real part of $Z_{11} - Z_{12}$ in the middle-frequency range

$$\mathrm{Im}(Z_{11} - Z_{12}) = R_{\mathrm{bx}} + R_{\mathrm{bi}}\frac{C_{\mathrm{bc}}}{C_s}. \tag{18}$$

It is also observed that the pad capacitances have a significant effect on the obtained value of $(R_{\mathrm{bx}} + R_{\mathrm{bi}}(C_{\mathrm{bc}}/C_s))$. The maximum variations of $(R_{\mathrm{bx}}+R_{\mathrm{bi}}*(C_{\mathrm{bc}}/C_s))$ before and after deembedding pad capacitances are 5 and 0.5, respectively. The result, after removing the pad parasitics, is shown in Fig. 12. This value is used to constrain the optimization procedure in order to obtain accurate values of R_{bx} and R_{bi}. The variation of $(R_{\mathrm{bx}}+R_{\mathrm{bi}}(C_{\mathrm{bc}}/C_s))$ is due to the change of C_{bc} with the

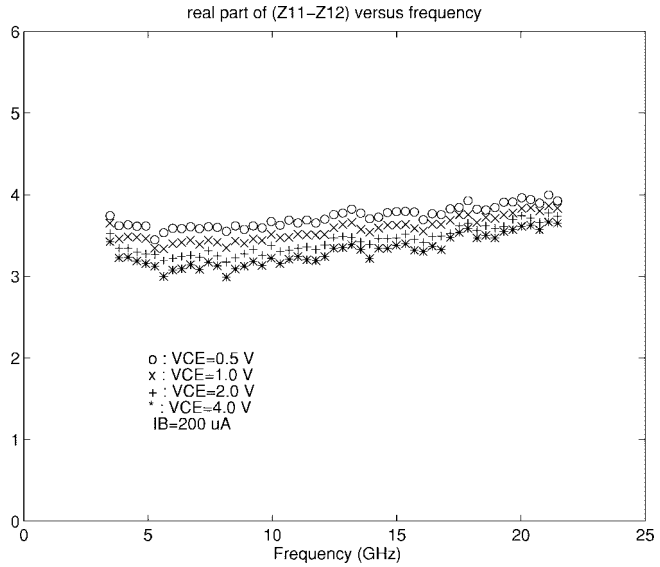

Fig. 12. The values of $R_{\rm bx} + R_{\rm bi}(C_{\rm bc}/C_s)$ after deembedding the pad capacitances.

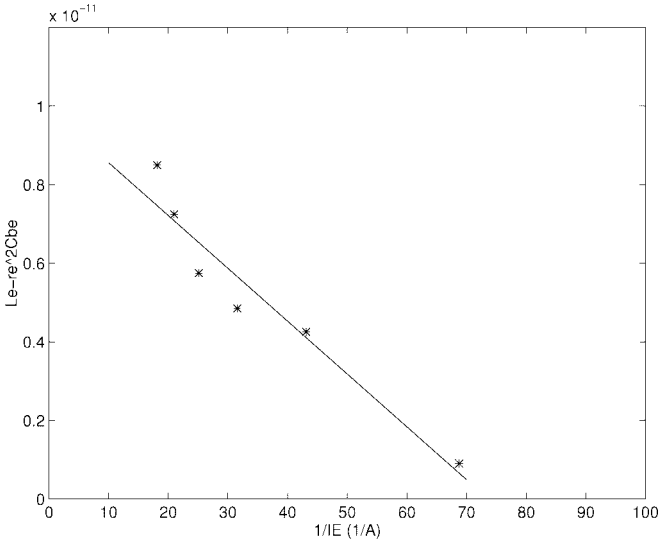

Fig. 13. $L_e - r_e^2 C_{\rm be}$ versus the inverse emitter current. $L_e = 9.99$ pH.

base–collector voltage $V_{\rm CE}$. $C_{\rm bc}$ decreases as $V_{\rm CE}$ increases. This causes the ratio $C_{\rm bc}/(C_{\rm bc}+C_f)$ to decrease and, hence, the magnitude of $(R_{\rm bx}+R_{\rm bi}(C_{\rm bc}/C_s))$ decreases.

H. The Emitter Resistance R_E and Base–Emitter Resistance r_e

$(R_E + r_e)$ can be obtained from the real part of Z_{12} in the middle-frequency range. With the high collector current where the neutral base recombination is the dominant recombination, $R_E + r_e$ can be expressed as

$$R_E + r_e = R_E + \frac{n_f kT}{qI_E}. \tag{19}$$

The real part of Z_{12} in the middle-frequency range is the sum of $(r_e + R_E)$. The plot of $(r_e + R_E)$ versus $1/I_E$ would give the values of R_E, r_e, and ideality factor n_f.

I. The Emitter Lead Inductor and Base–Emitter Capacitance

$L_e - C_{\rm be} r_e^2$ can be obtained from the imaginary part of Z_{12} in the lower middle-frequency range. In the case of high collector currents, the fraction of the depletion capacitance in the base–emitter capacitance $C_{\rm be}$ is small and $C_{\rm be}$ can be approximated to be proportional to I_E, and we also have $r_e \propto 1/I_E$. Therefore, the Y intercept of plot $L_e - r_e^2 C_{\rm be}$ versus $1/I_E$ gives the value of L_e. The value of $L_e - C_{\rm be} r_e^2$ at $f = 5$ GHz is used for this purpose. The plot of $L_e - C_{\rm be} r_e^2$ versus $1/I_e$ is shown in Fig. 13. The extracted value of L_e is 9. 95 pH.

Based on the values of L_e and r_e obtained previously, the value of $C_{\rm be}$ can be easily calculated. The value of $C_{\rm be}$ obtained in this way only serves to give the initial value of $C_{\rm be}$. An accurate value of $C_{\rm be}$ is obtained from the optimization procedure. It is noted that the magnitude of $C_{\rm be}$ is not sensitive to the optimization procedure. This is also reported in [7], where the value of $C_{\rm be}$ is calculated from f_α (where f_α is the transport factor α cutoff frequency and $f_\alpha = 1/r_e C_{\rm be}$). An accurate value of $C_{\rm be}$ is extremely difficult to obtain since changing the value of $C_{\rm be}$ does not change the error of optimization much over the bias ranges of the device under investigation.

J. The Transport Factor α

The transport factor α can be calculated directly by

$$\alpha = \frac{Z_{21} - Z_{12}}{Z_{22} - Z_{21} - R_c - j\omega L_c}. \tag{20}$$

Assuming a single-pole approximation, one can write

$$\alpha = \frac{\alpha_0}{1 + j\omega/\omega_\alpha} e^{-j\omega\tau} \tag{21}$$

where ω_α can be expressed as

$$\omega = \frac{1}{C_{\rm be} r_e} = \frac{1}{\tau_b} \tag{22}$$

τ_b is the base transit time and is related to physical parameters by $W_{\rm BC}^2/2D_n$ for n-p-n HBT's.

The magnitude of $\alpha(\omega)$ at $I_B = 200$ μA with different collector–emitter voltages is shown in Fig. 14. The fitted curve of the magnitude of α is also given in the plots. α_0 is obtained by taking the value of $|\alpha|$ at low frequency. ω_α (and, therefore, the base transit time $\tau_b = 1/\omega_\alpha$) can be calculated directly at each frequency using

$$\tau_b = \frac{\sqrt{\alpha_0^2 - |\alpha(\omega)|^2}}{\omega|\alpha(\omega)|}. \tag{23}$$

The calculated τ_b at $I_B = 200$ μA with different collector–emitter voltages is shown in Fig. 15. Since the base is heavily doped, the base-width modulation effect in the HBT's is negligible and, therefore, τ_b should be a weak function of I_B and $V_{\rm CE}$. The dependence of τ_b on the base current and collector–emitter voltage is not completely understood at this time. One possible reason for the α dependence on $V_{\rm CE}$ is the self-heating effect in the HBT's. The diffusion coefficient $D_n = (KT/q)\mu_n$ is a function of the temperature in which $\mu_n \propto T^{-s}$. An often quoted value of s is 2.3 (for the intrinsic

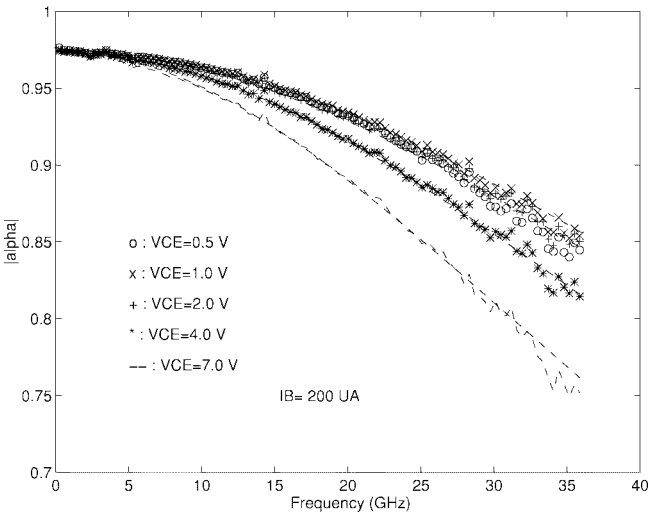

Fig. 14. $|\alpha|$ versus frequency at different collector–emitter voltages.

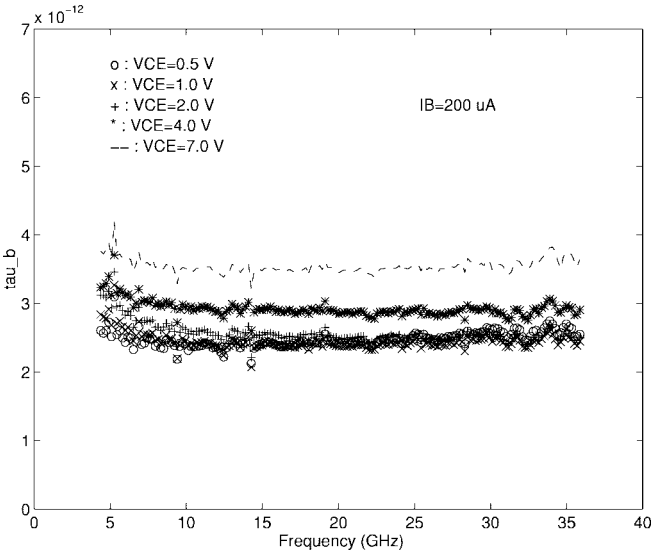

Fig. 15. τ_b versus frequency at different collector–emitter voltages.

GaAs). It is noted that the D_n decreases when the dissipated power in the HBT's increases. Therefore, the τ_b increases with the larger $V_{\rm CE}$.

The emitter–collector phase-delay time can be calculated by

$$\tau = \frac{1}{\omega}\left[-\angle\alpha(\omega) - \tan^{-1}\left(\omega/\omega_\alpha\right)\right] \tag{24}$$

where $\tau = (m/1.2)\tau_b + \tau_c$ and $m \simeq 0.22$.

The calculated τ versus frequency at $I_B = 200\ \mu$A with different values of $V_{\rm CE}$ is shown in Fig. 16. When the collector–emitter voltage increases, the collector transit time $\tau_c = W_{\rm BC}/2v_{\rm sat}$ increases due to the larger base–collector space region. Therefore, the emitter–collector delay time increases as expected with the larger collector–emitter voltage.

IV. Results and Discussion

The values of the bias-independent elements are given in Table I.

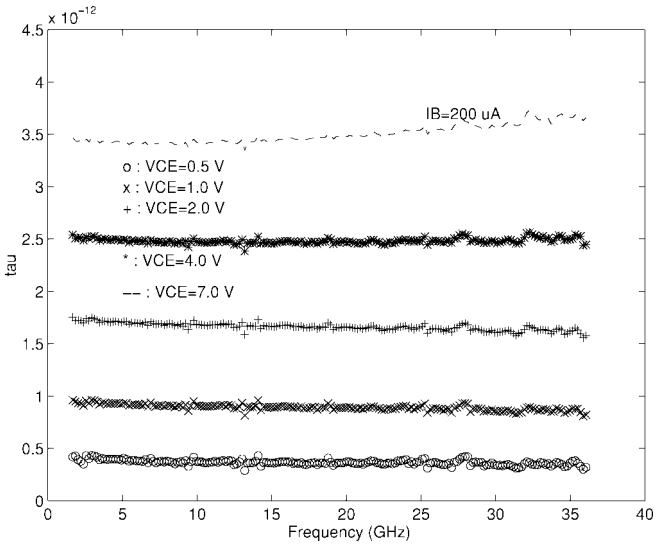

Fig. 16. τ versus frequency at different collector–emitter voltage.

TABLE I
Bias-Independent Parameters

Parameters	Values (analytical)	Values (optimized)
C_{pbc} (fF)	0	0
C_{pbe} (fF)	27.4	27.4
C_{pce} (fF)	41	42
C_f (fF)	16.5	16.5
L_b (pH)	55	55
L_e (pH)	9.9	5.46
L_c (pH)	61	61
$R_{bx}(\Omega)$	1.38	1.42
$R_{bi}(\Omega)$	2.3	4.049
$R_E(\Omega)$	1.832	1.832
$R_c(\Omega)$	4.99	4.99
error	2.2 %	0.43 %

All of the bias-independent elements are extracted from the procedure described above, except for L_e, $R_{\rm bi}$, and $R_{\rm bx}$. Accurate values of L_e, $R_{\rm bx}$, and $R_{\rm bi}$ are obtained from the empirical optimization procedure. Let $a = R_{\rm bx} + R_{\rm bi}(C_{\rm bc}/C_s)$ and $\gamma = C_{\rm bc}/C_s$. The initial values of $R_{\rm bi}$ and $R_{\rm bx}$ are estimated from the variation of a. We have $R_{\rm bx} = (\Delta a/\Delta\gamma)$. The calculated values of $R_{\rm bx}$ and $R_{\rm bi}$ are listed in Table I.

Instead of defining just the absolute and relative errors, the mixed relative and absolute errors are used to obtain the best fit between the measurement and simulation. The optimization error is defined by

$$E = 1/4N\sum_{i=1}^{N}\left[\left(\frac{S_{11}^{\rm mea} - S_{11}^{\rm sim}}{S_{11}^{\rm mea}}\right)^2 + \left(\frac{S_{12}^{\rm mea} - S_{12}^{\rm sim}}{S_{12}^{\rm mea}}\right)^2 + \left(S_{21}^{\rm mea} - S_{21}^{\rm sim}\right)^2 + \left(\frac{S_{22}^{\rm mea} - S_{22}^{\rm sim}}{S_{22}^{\rm mea}}\right)^2\right] \tag{25}$$

where N is the number of frequency points.

The errors between the measured and simulated S-parameters are also listed in Table I. The optimization was carried out at the bias $I_B = 200\ \mu$A and $V_{\rm CE} = 2.0$ V. It is shown that the error between the measurement and simulation at the bias $I_B = 200\ \mu$A, $V_{\rm CE} = 2.0$ V before the

TABLE II
BIAS-DEPENDENT PARAMETERS

V_{CE} (V)	0.50000	1.0000	2.0000	4.0000	7.0000
I_C (mA)	6.0	6.2	6.1	5.9	5.6
C_{bc} (fF)	109.1	64.75	41.50	26.8	18.70
$r_e(\Omega)$	4.168	4.0432	4.218	4.518	5.018
$R_{bc}(k\Omega)$	8.6	70	121	180	200
α_0	0.9741	0.9751	0.9751	0.9740	0.9740
C_{be}^A (fF)	344	344	344	344	344
f_α^A (GHz)	63	66	66	55	45
τ^A (ps)	0.42	0.95	1.7	2.52	3.42
C_{be}^O (fF)	289	238	239	268	293
f_α^O (GHz)	58.2	58.9	52.3	47.10	39.9
τ^O (ps)	0.158	0.69	1.09	2.08	3.14
$error^A$	0.98 %	0.84 %	0.86 %	0.62 %	0.9 %
$error^O$	0.50%	0.69 %	0.43%	0.41%	0.56%

TABLE III
BIAS-DEPENDENT PARAMETERS

I_B μ(A)	200.000	400.000	600.000	800.000	1000.000
I_C (mA)	6.1	14.1	22.6	30.19	38.8
C_{bc} (fF)	41.50	37.4	32.7	28.75	27.15
$r_e(\Omega)$	4.218	1.798	1.133	0.8482	0.6912
$R_{bc}(k\Omega)$	200	200	200	200	200
α_0	0.9751	0.9785	0.9796	0.9790	0.9790
C_{be}^A (fF)	344	863	1275	1704	2190
f_α^A (GHz)	66	72	94	114	102
τ^A (ps)	1.7	1.6	1.52	1.73	1.2
C_{be}^O (fF)	0.239	0.682	1.070	1.537	1.984
f_α^O (GHz)	52.3	64.4	79.1	88.9	81.2
τ^O (ps)	1.09	1.02	0.98	0.68	0.45
$error^A$	0.86 %	2.6 %	3.2 %	5.2 %	7.6 %
$error^O$	0.43 %	0.62 %	1.1 %	2.1 %	2.9%

optimization is already 2.2%. The bias-dependent parameters $C_{\rm be}$, r_e, $C_{\rm bc}$, $R_{\rm bc}$, α_0, f_α, and τ at constant base current $I_B = 200\ \mu$A and $V_{\rm CE} = \{0.5\,{\rm V}, 1.0\,{\rm V}, 2.0\,{\rm V}, 4.0\,{\rm V}, 7.0\,{\rm V}\}$ are given in Table II. Superscript A represents the results from optimization; Superscript O represents the results from the direct analysis.

Once the values of the bias-independent elements are known, all the bias-dependent values can be easily calculated and no further optimization is needed. It is shown in Table II that by using the directly calculated values of the bias-dependent elements, the error between simulation and measurement are very small. All the errors are less than 1%. Optimizations are also used. Only the three elements $C_{\rm be}$, f_α, and τ are optimized. The errors after optimization are given in the Table II. The variation of r_e is dependent on the collector current and self-heating effect. As explained previously, accurate values of $C_{\rm be}$ are very difficult to be obtain. The variation of $C_{\rm be}$ may result from the numerical techniques. The bias-dependent parameters $C_{\rm be}$, r_e, $C_{\rm bc}$, $R_{\rm bc}$, α_0, f_α, and τ at constant collector–emitter voltage $V_{\rm CE} = 2.0\,{\rm V}$ and $I_B = \{200\ \mu$A, 400 μA, 600 μA, 800 μA, and 1000 μA$\}$ are given in Table III.

The errors in using both the analytical approach and optimization procedure based on the initial values obtained from the analytical approach are given. It is shown that the errors obtained by using the analytical approach become higher if the collector currents increase. This is because the self-heating effect becomes more significant when the collector currents increase. However, the bias-independent elements are forced to be fixed in all the extraction procedures, and they are practically functions of the device temperature. The

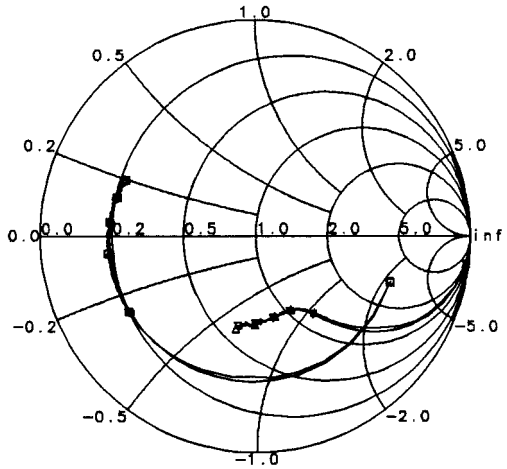

Fig. 17. The simulated and measured S_{11} and S_{22}. ∘: measured S_{11}, □: simulated S_{11}, ∇: measured S_{22}, △: measured S_{22}.

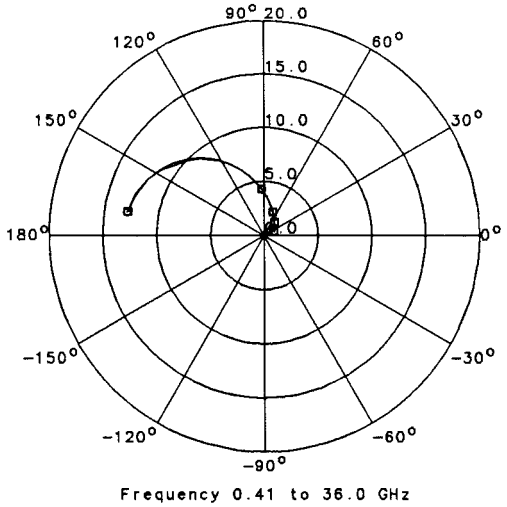

Fig. 18. The simulated and measured S_{21}. ∘: measured S_{21}, □: simulated S_{21}.

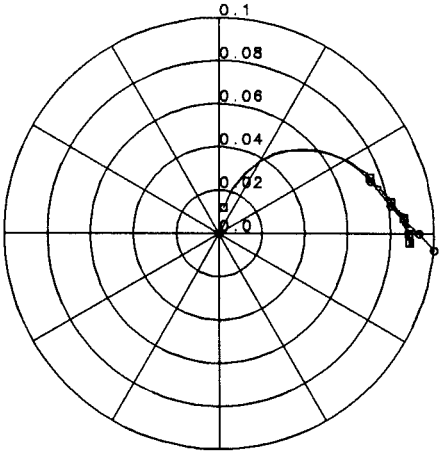

Fig. 19. The simulated and measured S_{12}. ∘: measured S_{12}, □: simulated S_{12}.

thermal effect is absorbed by the bias-dependent elements after optimization. Thus, the errors become smaller. As expected, $C_{\rm be}$ increases with increased collector currents. It is observed from Table III that $C_{\rm bc}$ decreases with the increased collector currents. This is not clearly understood at this time. One possible reason is the self-heating effect and modification of the base–collector-space charge region by the injected carriers [7].

The simulated and measured S-parameters at the bias $I_B = 200\ \mu$A and $V_{\rm CE} = 2.0$ V are shown in Figs. 17–19. The fit between the measured and modeled data is excellent.

V. Conclusion

A parameter-extraction procedure for the HBT's combining the analytical and optimization approach has been developed in this paper. The pad capacitances are extracted from the HBT's under cutoff operation. Most of the elements are obtained from the analysis of the behavior of the Z-parameters. The values of uncertain elements are obtained from the optimization at a specific bias. The initial values of these uncertain elements are also obtained from the analytical approach. The agreement between measurement and simulation over a range of bias values shows the validity of this approach.

Acknowledgment

The authors wish to thank Prof. C. G. Fonstad, Massachusetts Institute of Technology (MIT), Cambridge, for providing the use of laboratory facilities for this work.

References

[1] D. Costa, W. Liu, and J. S. Harris, Jr., "Direct extraction of the AlGaAs/GaAs heterojunction bipolar transistor small-signal equivalent circuit," *IEEE Trans. Electron Devices,* vol. 38, pp. 2018–2024, Sept. 1991.

[2] D. R. Pehlke and D. Pavlidis, "Evaluation of the factors determining HBT high-frequency performance by direct analysis of s-parameter data," *IEEE Trans. Microwave Theory Tech.,* vol. 40, pp. 2367–2373, Dec. 1992.

[3] U. Schaper and B. Holzapfl, "Analytical parameter extraction of the HBT equivalent circuit with T-like topology from measured s-parameters," *IEEE Trans. Microwave Theory Tech.,* vol. 40, pp. 493–498, Mar. 1995.

[4] S. J. Spiegel, D. Ritter, R. A. Hamm, A. Feygenson, and P. R. Smith, "Extraction of the InP/GaInAs heterojunction bipolar transistor small-signal equivalent circuit," *IEEE Trans. Electron Devices,* vol. 42, pp. 1059–1064, June 1995.

[5] J. M. M. Rios, L. M. Lunardi, S. Chandrasekhar, and Y. Miyamoto, "A self-consistent method for complete small-signal parameter extraction of InP-based heterojunction bipolar transistors (HBT's)," *IEEE Trans. Microwave Theory Tech.,* vol. 45, pp. 39–45, Jan. 1997.

[6] C.-J. Wei and J. C. M. Huang, "Direct extraction of equivalent circuit parameters for heterojunction bipolar transistors," *IEEE Trans. Microwave Theory Tech.,* vol. 43, pp. 2035–2039, Sept. 1995.

[7] A. Samelis and D. Pavlidis, "DC to high-frequency HBT-model parameter evaluation using impedance block conditioned optimization," *IEEE Trans. Microwave Theory Tech.,* vol. 45, pp. 886–897, June 1997.

[8] S. Lee and A. Gopinath, "Parameter extraction technique for HBT equivalent circuit using cutoff mode measurement," *IEEE Trans. Microwave Theory Tech.,* vol. 40, pp. 574–577, Mar. 1992.

[9] Y. Gobert, P. J. Tasker, and K. H. Bachem, "A physical, yet simple, small-signal equivalent circuit for the heterojunction bipolar transistor," *IEEE Trans. Microwave Theory Tech.,* vol. 45, pp. 149–153, Jan. 1997.

Bin Li (S'86) received the B.S. and M.S. degrees from Nanjing University, Nanjing, People's Republic of China, in 1985 and 1988, respectively, and the Ph.D. degree from Northeastern University, Boston, MA, in 1998.

He is currently with Vitesse Semiconductor Corporation, Camarillo, CA. His research has been in the area of modeling and simulation of HBT characteristics at microwave frequencies.

Sheila Prasad (SM'82) received the B.Sc. degree from the University of Mysore, India, and the S.M. and Ph.D. degrees in applied physics from Harvard University, Cambridge, MA.

She has been on the faculty of the Department of Electrical Engineering, New Mexico State University, Las Cruces, and the Department of Electrical and Electronics Engineering, Birla Institute of Technology and Science, Pilani, India. She is currently a Professor in the Department of Electrical and Computer Engineering, Northeastern University, Boston, MA. Her areas of research interests include microwave semiconductor devices, microwave solid-state circuits, and optoelectronics. She co-authored *Fundamental Electromagnetic Theory and Applications*.

Dr. Prasad is a member of Sigma Xi.

Li-Wu Yang (M'86–SM'96), photograph and biography not available at the time of publication.

S. C. Wang photograph and biography not available at the time of publication.